# Enhancing Charge Transport in Supramolecular Semiconductors by Strategic Hydrogen-Bonding Positioning

[a]Gabriel Martinez, [a,b,c]Kyeong-Im Hong, [d]Wakana Matsuda, [b]Carmen Munuera, [d]Shu Seki, [a,b,*]Amparo Ruiz-Carretero

[a]Gabriel Martínez, Kyeong-Im Hong, Amparo Ruiz-Carretero. University of Strasbourg, Institute Charles Sadron, CNRS, UPR22, 23 Rue du Loess, 67034, Strasbourg Cedex 2, France

[b]Instituto de Ciencia de Materiales de Madrid, Consejo Superior de Investigaciones Científicas CSIC, Sor Juana Inés de la Cruz 3, 28049, Madrid, Spain

[c]Current affiliation: Instituto Madrileño de Estudios Avanzados en Nanociencia (IMDEA Nanociencia), Calle Faraday 9, 28049, Madrid, Spain

[d] Dr. W. Matsuda, Prof. S. Seki. Department of Molecular Engineering, Graduate School of Engineering, Kyoto University, Nishikyo-ku, Kyoto 615-8510, Japan

*Corresponding author

E-mail: amparo.ruiz@ics-cnrs.unistra.fr

## Abstract

Hydrogen-bonded semiconductors stand among the next generation of electronic materials thanks to their promising and versatile properties. Hydrogen-bonding has been proven to effectively compete with traditional π-π stacking, yielding well-connected structures that enhance device morphology and electrical performance. Nevertheless, the precise positioning of hydrogen-bonding units within the molecular structure of π-conjugated segments, can significantly shape the supramolecular architectures that dictate the pathways for charge carriers and ultimately, device efficiency. We elucidate this scenario by exploring diketopyrrolopyrrole (DPP) molecules featuring amide units strategically positioned at varying distances from the DPP core. Using a comprehensive combination of spectroscopy, structural

1

and microscopy tools, we rationalize the charge transport properties through a contactless technique. Our results reveal that the proximity of the amide units to the DPP core governs the suppression or promotion of intermolecular hydrogen-bonding, resulting in materials exhibiting distinct crystalline or amorphous structures, along with divergent values of photoconductivity and charge carrier lifetimes. More importantly, the strategic positioning of hydrogen-bonding units represents the next step towards integrating hydrogen-bonded small molecules into practical optoelectronic devices.

**Key words**

Supramolecular electronics; hydrogen-bonding; charge transport; organic electronics

**Introduction**

In the rapidly evolving field of organic semiconductors, hydrogen-bonded materials have emerged as a class of compounds with promising electronic properties and tunable functionalities.[1–6] Among these, small molecules incorporating both, conjugated cores and hydrogen-bonding units, have gained significant attention for their unique characteristics and potential applications in electronic devices.[2,7,8] One crucial aspect influencing the performance of such materials is the distance between the conjugated core and the hydrogen-bonding unit.[9–11] This parameter not only governs the self-assembly and crystalline packing of these molecules but also plays a pivotal role in determining the charge transport properties within the semiconductor. The interplay between the electronic structure of the conjugated core and the strength and orientation of hydrogen-bonding introduces a delicate balance that can be finely tuned through the manipulation of intermolecular distances. Literature reports have previously demonstrated the role of the alkyl linker length in the supramolecular self-assembly structures and the charge carrier mobilities. For instance, the variation of the alkyl chain spacer connecting N-annulated perylenebisimides (N-PBIs) to amide-containing peripheral side chains, resulted in structures leading to pathway complexity or kinetically trapped species depending on the length of the spacer.[10] In another exciting example, [1]benzothieno[3,2-*b*][1]benzothiophene (BTBT) molecules were

2

disubstituted with aliphatic chains containing terminal hydroxy groups.[9] The evaluation of the electronic properties revealed a strong relationship between charge carrier mobility and the number of carbons of the aliphatic chains. The authors found out a remarkable odd-even effect with the odd series consistently displaying significant higher mobility values in organic field effect transistors (OFETs) as a result of the modulation of the orientation of lamellar structures *via* hydrogen-bonding formation.

In this work, we investigate the impact of varying distances between the conjugated core and the hydrogen-bonding unit on the structural and optoelectronic properties of amide-containing semiconductors based on diketopyrrolopyrrole[12,13] (DPP) derivatives. Through a series of three small molecules, **HDPPBA-2C**, **HDPPBA-4C** and **HDPPBA-6C** (Scheme 1), built on thiophene-capped DPP with controlled distances between the conjugated core and amide units as the hydrogen-bonding moieties, we seek to establish a fundamental understanding of how these structural variations influence charge carrier mobility, photophysical characteristics, and overall device performance. We have intentionally chosen this molecular design (Scheme 1) based on our previous results showing superior charge transport properties when the DPP derivatives were functionalized on the lactam positions *vs* the thiophene rings.[14] The promotion or suppression of intermolecular hydrogen-bonding dictates the final electronic performance, having important consequences in the formation of interconnected aggregates, even if small and disordered, a unifying requirement for high carrier mobility.[15,16] This fundamental relationship presented by Salleo *et al.* between short-range order in π-aggregates, aggregate connectivity, and macroscopic charge transport led us to further focus our attention in the nature, crystalline or amorphous, of the aggregated microstructures in the solid state.[15] Therefore, we show how the differences in linker's length from the hydrogen-bonding unit to the π-conjugated semiconducting segment render crystalline or amorphous structures, depending on the promotion or suppression of intermolecular hydrogen-bonding, resulting in dramatic changes in charge carrier mobility and lifetimes. We follow the self-assembly differences among the hydrogen-bonded compounds of the series in solution and on thin film with spectroscopy and structural methods, and explore the photoconductivity properties using an electrodeless technique. The outcomes of this research not only hold significance for the development of efficient organic semiconductor materials but also contribute to the broader understanding of the role of hydrogen-bonding in shaping the

3

electronic properties of functional molecular systems, even those based on particularly small molecules. Ultimately, our findings aim to provide valuable insights that can guide the rational design of hydrogen-bonded semiconductors, opening new avenues for the progress of organic optoelectronics.

**Results and discussion**

*Synthesis*

Compounds **1** and **HDPPBA-6C** were synthesized following a protocol previously reported by our group.[17] On the other hand, **HDPPBA-2C** and **HDPPBA-4C** (**Error! Reference source not found.**) were obtained starting from derivative **1**, and introducing the hydrogen-bonding motifs in subsequent steps (**Error! Reference source not found.**). Initially, product **1** was alkylated using *t*-butyl bromoacetate and *t*-butyl 4-bromobutanoate to afford **HDPP-2C-P** and **HDPP-4C-P** in 17% and 13% yield, respectively.[18] The low yields are attributed to the reduced solubility of the starting material **1** in acetone, in addition to the expected formation of *N,O*- and/or *O,O'*- alkylated isomers as byproducts.[19] Then, a deprotection step was performed using trifluoroacetic acid (TFA) to isolate **HDPP-2C-acid** and **HDPP-4C-acid** with 78% and 89% yield, respectively. Finally, the resulting diacids were functionalized with 1-decanamine and 1-octanamine through a peptide coupling reaction using hexafluorophosphate benzotriazole tetramethyl uronium (HBTU)[20] to obtain **HDPPBA-2C** and **HDPPBA-4C** in 79 and 89% yields, respectively. The final molecules were characterized by $^1$H, $^{13}$C-NMR and high-resolution mass spectrometry (see SI for detailed description and full characterization).

*Optical and self-assembly properties*

To investigate the role of hydrogen-bonding, the influence of their spatial positioning, and the interplay of noncovalent interactions on the optical and self-assembly properties, we have performed UV-Vis absorption, Fourier Transform Infrared (FTIR) and Nuclear Magnetic Resonance (NMR) spectroscopy studies at variable temperature (VT) and concentration in different solvents. UV-Vis, FTIR spectroscopy and X-ray diffraction on thin film helped us understanding the molecular packing and crystallinity of the samples.
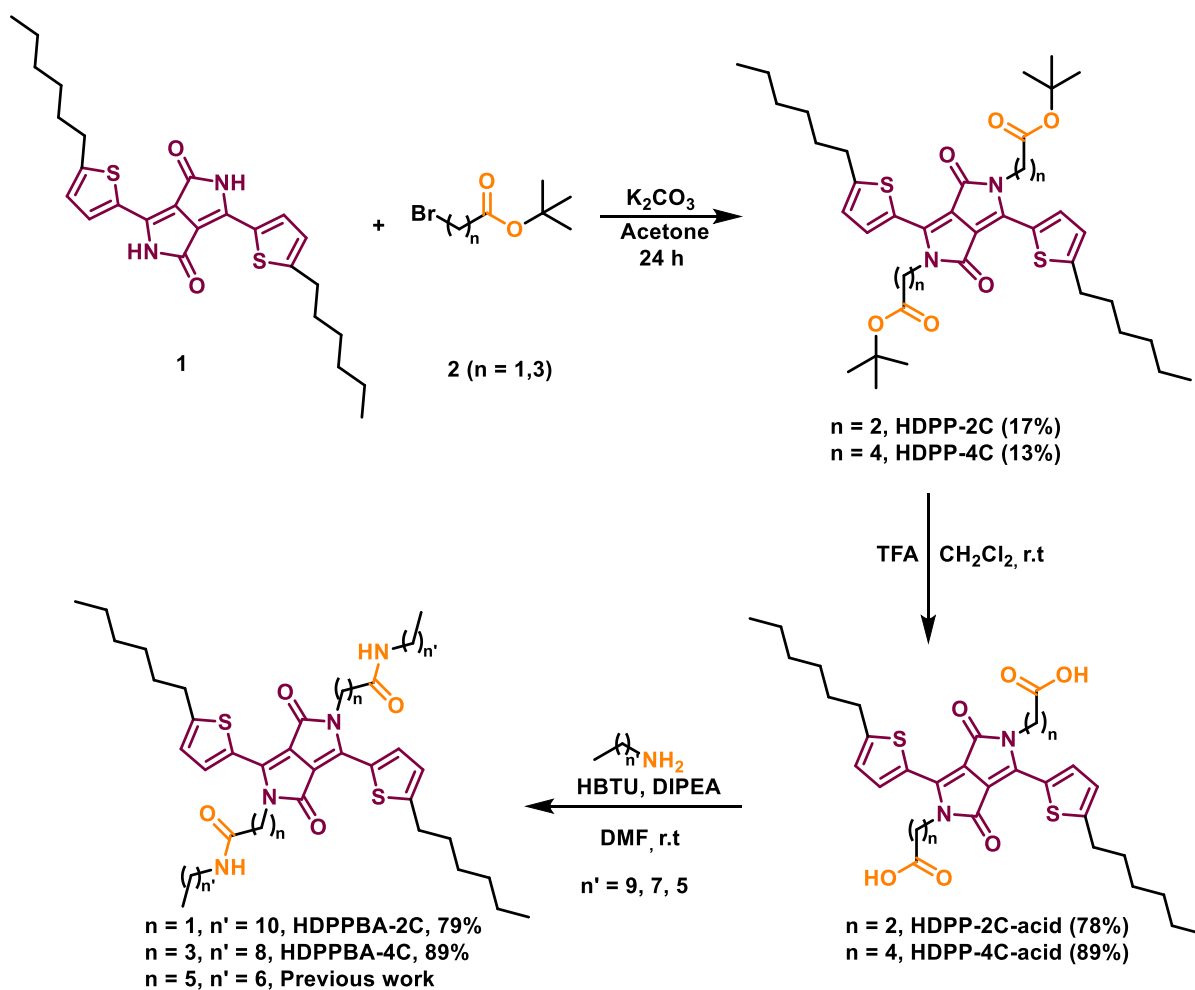
**Scheme 1.** Synthetic route towards **HDPPBA-2C** and **HDPPBA-4C**.

The UV-Vis spectra in chloroform ($CHCl_3$) solution of **HDPPBA-2C**, **HDPPBA-4C** and **HDPPBA-6C** at 20 °C show two main bands, characteristic of DPP dyes, having absorption maxima at λ = 520 nm and λ = 560 nm (Figure 1a). They are attributed to intramolecular charge transfer (ICT) transitions between the electron-rich and electron-poor units of the thiophene DPP system.[21] The comparable absorption spectra of the three derivatives in $CHCl_3$ is due to the good solubility of these chromophores in this solvent, limiting the formation of hydrogen-bonded structures at the concentration tested. Furthermore, in this solvent no evidence of aggregation was observed upon diluting the samples within the range of concentrations explored by UV-Vis absorption (Figure S1a-c).
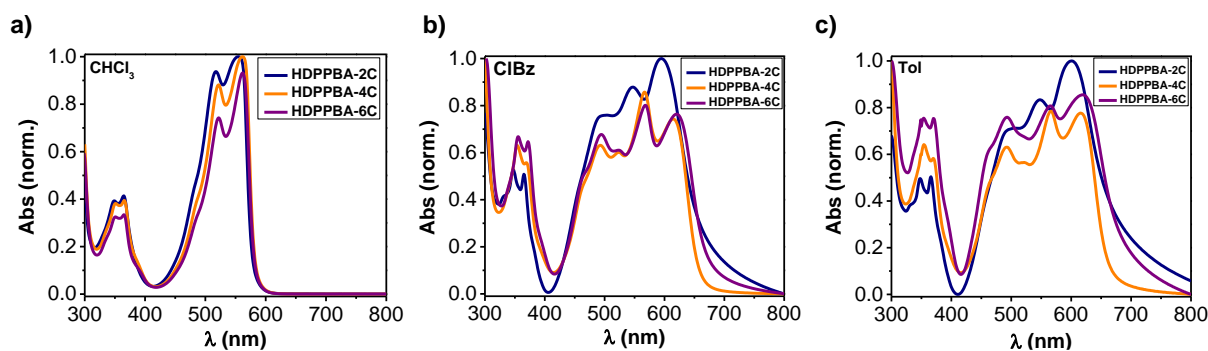
5

**Figure 1.** Absorption spectra of **HDPPBA-2C**, **HDPPBA-4C** and **HDPPBA-6C** in a) CHCl$_3$, b) Chlorobenzene (ClBz) and c) Toluene (Tol) at room temperature. [**HDPPBA-2C**] = [**HDPPBA-4C**] = [**HDPPBA-6C**] = 1.0 mg/ml in all cases.

We further explored the self-assembly behavior of the three derivatives by FTIR in CDCl$_3$ solution, being possible to increase the concentration further than when measuring UV-Vis absorption. We followed the most representative bands of the amide groups involved in hydrogen-bonding, such as the Amide A band, corresponding to N-H stretching, and that ranges between 3500 and 3250 cm$^{-1}$. In this area, lower Amide A frequencies evidence that hydrogen-bonding is present.[22–24] We studied solutions at 2.5 and 5 mg/ml in CDCl$_3$, finding that the three derivatives present hydrogen-bonding aggregation as shown by the peaks present between 3330 and 3290 cm$^{-1}$ (Figure 2a). **HDPPBA-2C** and **HDPPBA-6C** show bands of free amide groups at 2.5 mg/ml, while they are partially hydrogen-bonded at 5 mg/ml (Figure 2a), as demonstrated by the bands at 3293 cm$^{-1}$ and 3308 cm$^{-1}$, for **HDPPBA-2C** and **HDPPBA-6C**, respectively. Interestingly, **HDPPBA-4C** is partially hydrogen-bonded at both concentrations, presenting two bands at 3447 and 3326 cm$^{-1}$ (Figure 2a). The results are confirmed by the Amide I and amide II related to the C=O stretching mode (Figure 2b).

When using different solvents, such as chlorobenzene (ClBz) and toluene (Tol), commonly used in organic electronic device fabrication, additional absorption bands at lower and higher energies are observed by UV-Vis absorption for the three derivatives (**Error! Reference source not found.**b and 1c). **HDPPBA-2C**, **HDPPBA-4C** and **HDPPBA-6C** present bands at higher energies centered at 493 nm in ClBz (Figure 1b) and 491 nm in Tol (Figure 1c) for the three derivatives, attributed to the formation of H-type aggregates, mainly governed by π-π stacking interactions. On the other hand, bands

6

at lower energies are observed at 595, 615 and 620 nm in ClBz (**Error! Reference source not found.**b), and 600, 616 and 620 nm in Tol (**Error! Reference source not found.**c) for **HDPPBA-2C**, **HDPPBA-4C** and **HDPPBA-6C**, respectively. The appearance of these red-shifted bands under self-assembly conditions are due to the formation of J-type aggregates,[25] in which processes of intermolecular charge transfer between aggregated DPP units occur. In these aggregates the DPP units are self-assembled in a head-to-tail fashion as a result of intermolecular hydrogen-bonding thanks to the presence of the amide moieties.[26] We demonstrated the role of hydrogen-bonding in the formation of the aggregates by adding hydrogen-bonding disrupting solvents, such as methanol (MeOH). In this case, the J-aggregate bands disappeared upon addition of MeOH (Figure S2).
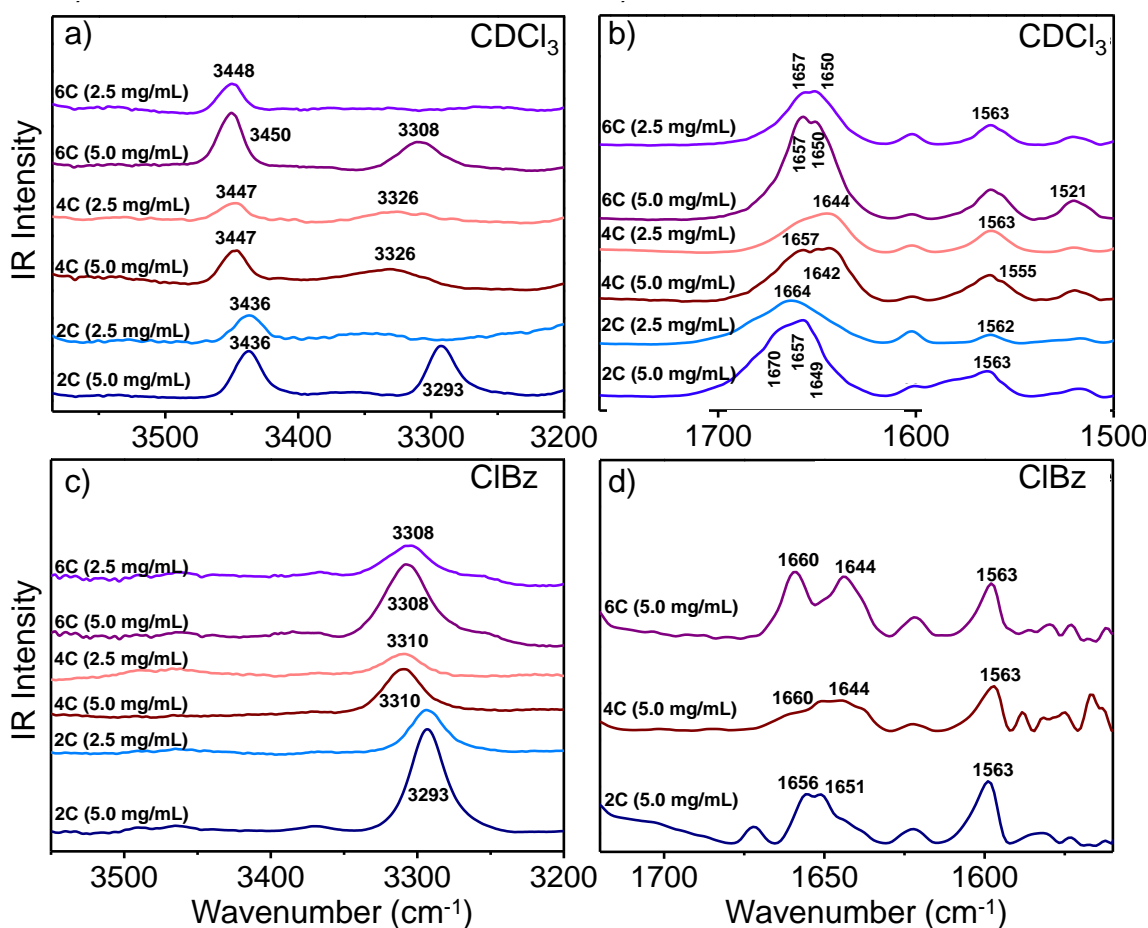


**Figure 2.** Solution FTIR Spectra in the Amide A (a) and Amide I and II regions (b) of **HDPPBA-2C**, **HDPPBA-4C** and **HDPPBA-6C** in CDCl₃ at 5.0 and 2.5 mg/ml. Solution FTIR Spectra Amide A (c)

and Amide I and II regions (d) of **HDPPBA-2C**, **HDPPBA-4C** and **HDPPBA-6C** in chlorobenzene

at 5.0 and 2.5 mg/ml.

We evaluated the degree of supramolecular aggregation by UV-Vis absorption varying the concentration of the ClBz and Tol solutions, and spectral differences were found among the three derivatives (Figure S1 d-i). **HDPPBA-2C** is the only derivative that presents a predominant J-aggregate band at $\lambda = 595$ nm over the whole range of concentrations tested (2.5 to 0.06 mg/ml) in ClBz and Tol (Figure S1d and S1g), showing minor spectral changes upon dilution in these two solvents. The same effect is not observed in **HDPPBA-4C** (Figure S1e and S1h) or **HDPPBA-6C** (Figure S1f and S1i), where the J-aggregate band decreases upon dilution until total disappearance at 0.06 mg/ml and 0.03 mg/ml in ClBz and Tol, respectively. These results point out to the different aggregation behavior of **HDPPBA-2C** with respect to the other two derivatives. It seems that the formation of intermolecular hydrogen bonds in **HDPPBA-4C** and **HDPPBA-6C**, responsible for the formation of J-type aggregates, is influenced by the solution preparation conditions, such as the concentration. This is not the case for **HDPPBA-2C**, possibly forming intramolecular hydrogen-bonding between the amide bond of the alkyl chain and the carbonyl of the DPP core (Scheme 2a), much less altered by external stimuli. Similarly, the H-aggregate band remarkably decreases for **HDPPBA-4C** and **HDPPBA-6C** compared to **HDPPBA-2C**, demonstrating the stronger aggregation tendency through $\pi-\pi$ stacking for **HDPPBA-2C** (Figure S1d and S1g), and supporting the formation of intramolecular hydrogen-bonding.

FTIR measurements also demonstrated the presence of hydrogen-bonding in ClBz solution (5.0 and 2.5 mg/ml) by showing only one amide A band ranging from 3308 cm$^{-1}$ and 3293 cm$^{-1}$ (Figure 2c). The difference in wavenumber shows the different aggregation patterns between **HDPPBA-2C** and the other two derivatives. This different behavior is also observed in the C=O vibration region, finding that **HDPPBA-4C** and **HDPPBA-6C** present a band at 1660 cm$^{-1}$ associated to the carbonyl group in the lactam ring, and another band at 1644 cm$^{-1}$, corresponding to the carbonyl group of the pending amide units engaged in strong hydrogen-bonding (Figure 2d). In contrast, **HDPPBA-2C** does not show these bands and instead, presents a broad band between 1656 cm$^{-1}$ and 1651 cm$^{-1}$, where both carbonyl (lactam and pending amide) bands overlap. This result clearly shows the different hydrogen-bonding

8

formation between **HDPPBA-2C** and the other two derivatives, as well as the different aggregates formed in ClBz and CDCl$_3$.
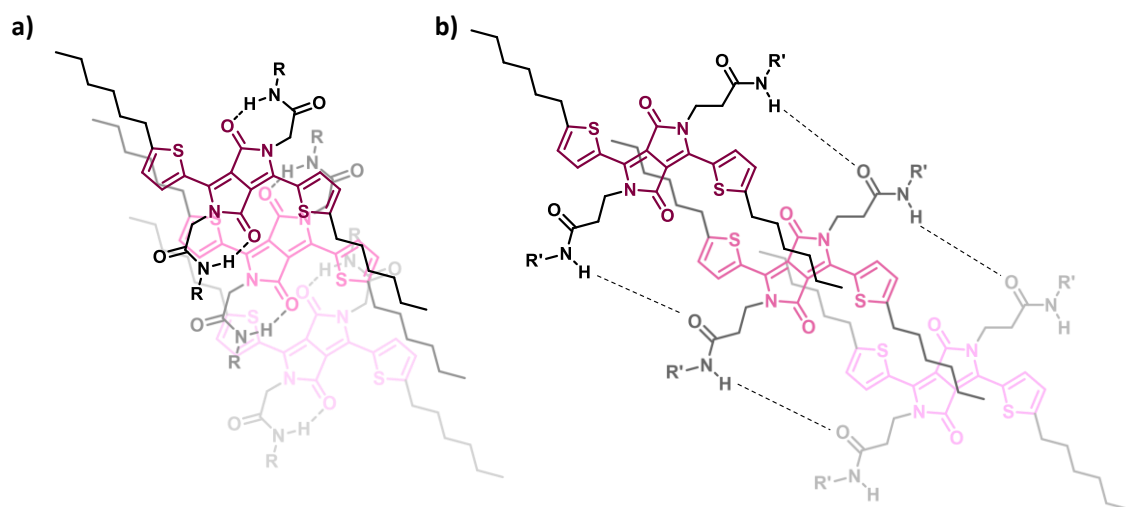


**Scheme 2.** Aggregation models proposed for a) **HDPPBA-2C** and b) **HDPPBA-4C** and **HDPPBA-6C**.

Likewise, VT UV-Vis absorption measurements confirmed the results observed at variable concentration UV-Vis (Figure S3). In this case, we explored ClBz and Tol solutions at a fixed concentration (1.0 mg/ml), and observed the spectral evolution upon heating from 20 to 100 °C. As expected, increasing the temperature causes the decrease of H- and J-aggregate bands, reaching the molecularly dissolved state at high temperature for the three derivatives (Figure S3). **HDPPBA-4C** and **HDPPBA-6C** have bands attributed to aggregated states in ClBz up to 40 °C and in toluene up to 60 °C (Figure S3b, S3c, S3e and S3f). Intriguingly, **HDPPBA-2C** showed aggregation bands still present at 60 °C in ClBz, and up to 80 °C in Tol (Figure S3a and S3d), suggesting that the self-assembled structures of this derivatives are less influenced by external stimulus, such as temperature.

Motivated by qualitatively unravelling the molecular packing of the different aggregates, and the interactions driving such arrangements in different solvents, we monitored the changes in the chemical shifts of **HDPPBA-2C**, **HDPPBA-4C** and **HDPPBA-6C** by $^1$H- (concentration and temperature variable) NMR experiments in CDCl$_3$ and toluene-$d$8.[27,28] Initially, the $^1$H-NMR spectra of the three

9

DPP derivatives were measured in CDCl$_3$ at 20 °C (Figure S4) at a sufficiently high concentration to assure the presence of hydrogen-bonding interactions (20 mM, 7.2 mg/ml). Interestingly, there are noticeable differences in the chemical shifts of the aromatic (*1* and *2*, Figure S4) and the amide protons (*3*, Figure S4) between the derivatives. **HDPPBA-4C** and **HDPPBA-6C** have aromatic protons with similar chemical shifts, whereas proton *2* (Figure S4) in **HDPPBA-2C** exhibits a significant upfield shift due to its spatial proximity to the carbonyl group in the lactam ring. Furthermore, there are even more noticeable shifts in the position of the amide proton *3*. These signals are sensitive to changes in the strength of hydrogen-bonding interactions in which the amide group is involved.[29,30] A stronger hydrogen-bonding interaction, as observed for **HDPPBA-4C**, results in a downfield shift of ~740 ppb compared to **HDPPBA-6C** (amide proton *3*, 5.52 *vs* 6.26 ppm). When we increased the concentration from 0.5 to 7.2 mg/ml in CDCl$_3$ (0.5 mM to 20 mM), the aromatic protons *1* and *2* of the three derivatives exhibit a shielding effect (Figure 3a, 3b and 3c) as a sign of stronger aggregation,[31–33] generated by the ring current of neighboring aromatic rings π-stacked in a face-to-face fashion and due to the proximal packing of the aromatic cores promoted by higher concentration.[34] Regarding amide proton *3*, we observe big differences between **HDPPBA-4C**, **HDPPBA-6C** and **HDPPBA-2C**. While there is a downfield shift of 35.05 and 47.42 ppb (Figure 3b and 3c, **Error! Reference source not found.**) upon increasing the concentration for **HDPPBA-4C** and **HDPPBA-6C**, **HDPPBA-2C** experiences a very modest deshielding (10.62 ppb, Figure 3a, Table S1). In the case of **HDPPBA-4C** and **HDPPBA-6C**, the downfield shift is explained by the decrease of electron density around the proton nucleus as a consequence of intermolecular hydrogen-bonding.[30] In contrast, the formation of hydrogen-bonding in **HDPPBA-2C** is not influenced by concentration changes as observed by FTIR and UV-Vis spectroscopies. A comparable behavior on the chemical shift of the amide protons has been previously described in intramolecularly hydrogen-bonded pseudocycles.[10,35] Consequently, the results in CDCl$_3$ at high concentrations suggest a self-assembly process that yields H-type aggregation driven by face-to-face π-π stacking, accompanied by intramolecular hydrogen-bonding in the case of **HDPPBA-2C** (Scheme 2a).[36–38] In contrast, intermolecular hydrogen-bonding occurs in the supramolecular structures formed by **HDPPBA-4C** and **HDPPBA-6C** (Scheme 2b). In a different set of experiments, we evaluated as well the temperature dependence on the chemical shifts of the three

10

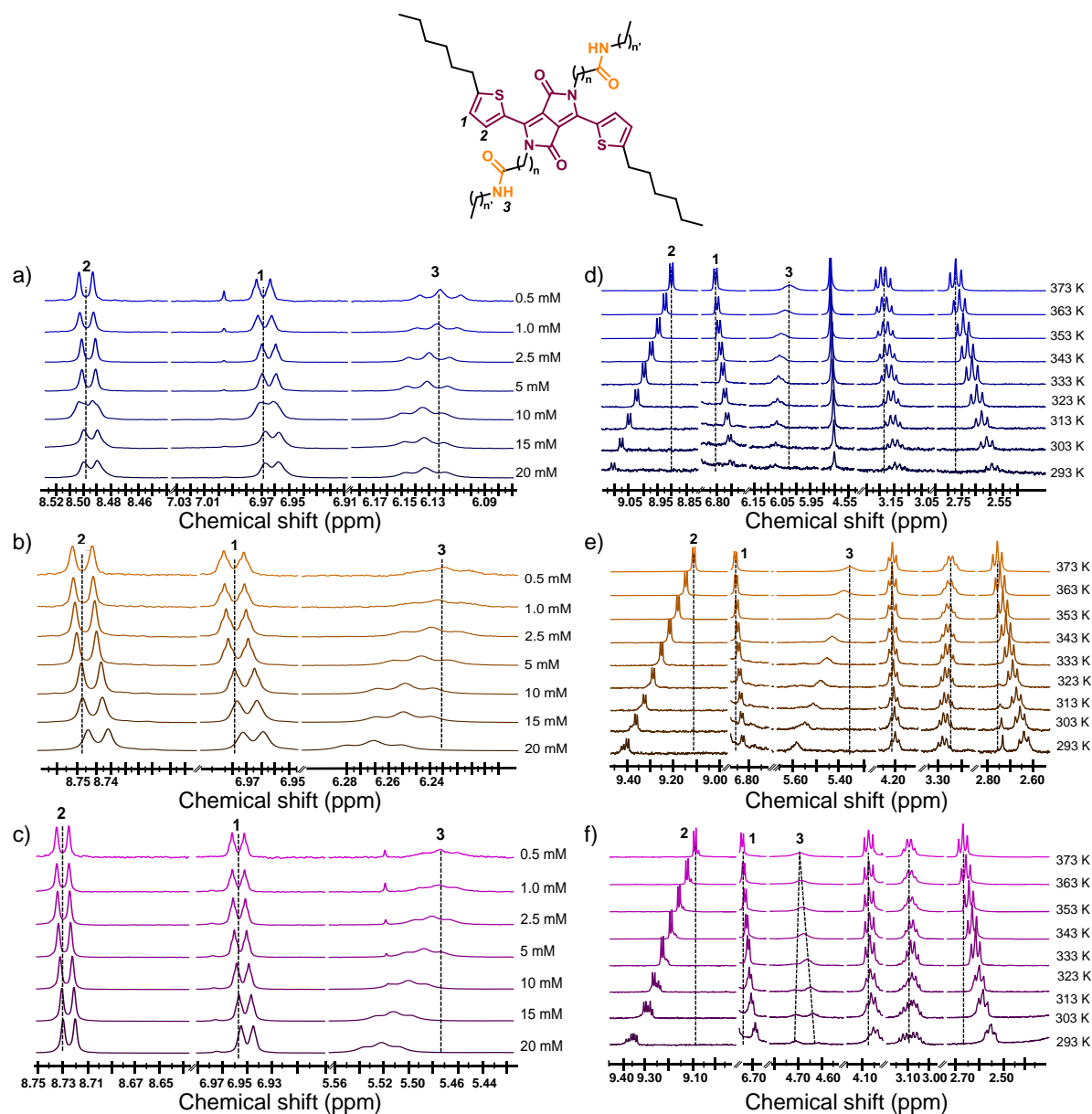derivatives in a low-polarity solvent, in which the formation of hydrogen-bonding interactions is favored.[39]



**Figure 3.** Concentration dependent $^1$H-NMR spectra of a) **HDPPBA-2C** b) **HDPPBA-4C** and c) **HDPPBA-6C** in Tol- *d8* (0.5 mM to 20 mM at 20 °C) and, temperature dependent $^1$H-NMR spectra of d) **HDPPBA-2C** e) **HDPPBA-4C** and f) **HDPPBA-6C** in Tol-*d8* (5 mM at 20 °C) showing the aromatic and amide proton region.

We conducted $^1$H-NMR in Tol-*d8* between 100 °C and 20 °C, a temperature range where all derivatives display UV-Vis absorption spectra of monomeric species at 100 °C, while they exhibit aggregation bands at 20 °C. As expected, the aromatic protons experience important shifts upon cooling for the three derivatives (Figure 3d, 3e and 3f). Remarkably, aromatic proton *2* (closer to the DPP core, Figure 3d, 3e and 3f) experiences a significant downfield shift (~ 200 ppb, **Error! Reference source not found.**) upon cooling. A phenomenon that is contrary to what is observed for π-π aggregated aromatic systems in a face-to-face fashion. In contrast, the aromatic proton *1* (Figure 3d, 3e and 3f) experiences an upfield shift (~ 50 ppb, **Error! Reference source not found.**). Furthermore, the self-assembly process induces a splitting of the aromatic protons at temperatures lower than 30 °C and 60 °C for **HDPPBA-4C** (Figure 3e) and **HDPPBA-6C** (Figure 3f), respectively, suggesting that the aromatic protons are not experiencing the same magnetic environment due to aggregation.[40] This effect is not seen for **HDPPBA-2C**. In addition, we noted that lowering the temperature causes shielding of the methylene protons (~ 2.6 ppm, **Error! Reference source not found.**, 3e and 3f) in the hexyl chains of the thiophenes. This is indicative of stronger van der Waals interactions occurring in the aggregated state of **HDPPBA-4C** and **HDPPBA-6C**.[10,41]

In summary, the aggregation processes studied by NMR in Tol-*d8* revealed self-assembled supramolecular structures that differ from the ones in CDCl$_3$. In Tol-*d8*, J-type aggregates are predominant, which would explain the difference in the shift of the aromatic protons upon aggregation compared to CDCl$_3$. In contrast, in the latter solvent, H-type aggregates are predominant, as previously described. Overall, the results indicate that **HDPPBA-2C** forms H-type aggregates in CHCl$_3$ at high concentrations, and J-type aggregates at lower concentration in Tol driven by π-π stacking and intramolecular hydrogen-bonding in both cases. Likewise, **HDPPBA-4C** and **HDPPBA-6C** self-assemble into H- and J-type aggregates in CHCl$_3$ and toluene, respectively, but in their case the self-assembly is driven by π-π stacking accompanied by intermolecular hydrogen-bonding.

In a last characterization step, we evaluated the frontier orbital energy levels for **HDPPBA-2C**, **HDPPBA-4C** and **HDPPBA-6C** to analyze their suitability for their application in organic electronic devices. We performed cyclic voltammetry measurements in dichloromethane and recorded the voltammograms after heating up the samples to eliminate the presence of macroscopic aggregates at the

concentration used (Figure S5). **HDPPBA-2C** displays a cyclic voltammogram with two one-electron oxidation peaks reversible in nature at $E_{1/2}$ 0.47 and $E_{1/2}$ 0.8 V accompanied by a one-electron reduction peak at $E_{pa}$ -1.55 V, which is irreversible. For **HDPPBA-4C**, two oxidation peaks at $E_{pc}$ 0.39 V and $E_{pc}$ 0.73 V were observed, both likely to be one-electron processes from the current magnitude, and neither showing any appreciable reversibility. An irreversible reduction peak was found at $E_{pa}$ -1.69 eV. Finally, **HDPPBA-6C** presented similar redox processes, showing quasi-reversible oxidation peaks at 0.38 V and 0.71 V, accompanied by a reversible reduction peak at -1.73 V. These results highlight that the three hydrogen-bonded derivatives are electron-rich since they demonstrate the ability to donate two electrons. The Highest Occupied Molecular Orbital (HOMO) and Lowes Unoccupied Molecular Orbital (LUMO) energy levels were calculated from the oxidation and reduction onset potentials, respectively and using ferrocene as a reference (Table S3). The HOMO levels of **HDPPBA-2C**, **HDPPBA-4C** and **HDPPBA-6C** were calculated to be -5.16, -5.10 and -5.08 eV, correspondingly. On the other hand, the obtained LUMO values were -3.43, -3.51 and -3.46 eV (See SI for details on the HOMO and LUMO calculations). In spite of the similarity of the alkyl chains in thiophenes and amide chains in the lactams, the electronic properties present appreciable differences. The closer proximity of the amide group to the DPP decreases the electron density of the derivative as evidenced by a first oxidation process at higher potential (0.47 V) and a larger band gap (1.73 eV). This phenomenon is less noticeable in derivatives where the amide moiety is positioned at distances of four and six carbons away from the DPP core, exhibiting lower band gaps. Therefore, varying the position of the hydrogen-bonding group within the conjugated systems is a technique to modulate the frontier orbital energy levels of $\pi$ conjugated systems.

*Photoconductivity studies*

We screened the charge transport properties of **HDPPBA-2C, HDPPBA-4C** and **HDPPBA-6C** using an electrodeless technique. Particularly, we prepared thin films of the three derivatives by drop casting CHCl$_3$ solutions, and measured the photoconductivity properties using Flash-Photolysis Time-Resolved Microwave Conductivity (FP-TRMC).[42,43] This technique provides a measure of photoconductivity as $\Phi\Sigma\mu$, where $\Phi$ is the charge carrier generation quantum yield and $\Sigma\mu$ is the sum of charge carrier

13

mobilities of electrons and holes. The thin films are irradiated with a pulsed laser generating charge carriers, being possible to follow their lifetimes before recombination. We had previously evaluated hydrogen-bonded derivatives made in our lab using this technique and therefore, it became the best tool to compare the results, as well as to compare to other hydrogen-bonded materials reported in the literature and measured with this technique.[44–47] The kinetic traces of conductivity transients are shown in figure 4a, and the calculated values of photoconductivity ($\phi\Sigma\mu$), rate constants ($k$, calculated 3 µs after pulse excitation) and half lifetime ($t_{1/2}$) are summarized in table 1. As figure 4a proves, **HDPPBA-4C** has the highest value of photoconductivity of the three derivatives ($3.5 \times 10^{-5}$ cm$^2$ V$^{-1}$ s$^{-1}$, Table 1), being **HDPPBA-2C** the least performing derivative of the series, not only having lower value of photoconductivity ($1.5 \times 10^{-5}$ cm$^2$ V$^{-1}$ s$^{-1}$), but one order of magnitude faster recombination time (Table 1) compared to **HDPPBA-4C** and **HDPPBA-6C**. **HDPPBA-6C** had an intermediate photoconductivity value of $2.8 \times 10^{-5}$ cm$^{-2}$V$^{-1}$s$^{-1}$ (Figure 4a), which indicates that the ability to efficiently transport charges is not linearly related to the proximity of the H-bonding unit to the DPP core.

We ran structural measurements on the devices' thin films to rationalize the photoconductivity results. FTIR measurements revealed amide A bands at 3291 cm$^{-1}$ for **HDPPBA-2C** and 3308 cm$^{-1}$ for **HDPPBA-4C** and **HDPPBA-6C**, which are values comparable to the ones found in chlorobenzene solution (Figure 4b), were the derivatives are aggregated by strong hydrogen-bonding. In the carbonyl vibration region, **HDPPBA-4C** and **HDPPBA-6C** show one peak at 1644 cm$^{-1}$, corresponding to the amide I band of amides engaged in strong hydrogen-bonding (Figure 4b), and the band corresponding to the carbonyl of the lactam rings at 1660 cm$^{-1}$. On the contrary, **HDPPBA-2C** has a peak at 3291 cm$^{-1}$ in the amide A region, indicating strong hydrogen-bonding as well. Nevertheless, there is only a predominant wide band at 1660 cm$^{-1}$ and no bands showing amide units engaged in intermolecular hydrogen-bonding (Figure 4b). In fact, the spectrum of **HDPPBA-2C** resembles the spectrum of a control DPP derivative (Figure 4b and Figure S6) unable to form intermolecular hydrogen bonds.[17] Still, the band at 1660 cm$^{-1}$ for **HDPPBA-2C** is quite broad, probably due to the overlapping of the amide unit band. These results confirm that **HDPPBA-2C** forms an intramolecular hydrogen-bond between the amide protons of the alkyl chain and the carbonyl in the lactam of the DPP core (Scheme 2a). In this sense, the band attributed to intramolecular hydrogen-bonding has been proven to be shifted

14

towards higher frequencies compared to the C=O stretching band of intermolecular hydrogen-bonding previously reported, [48,49] which agrees with our findings.
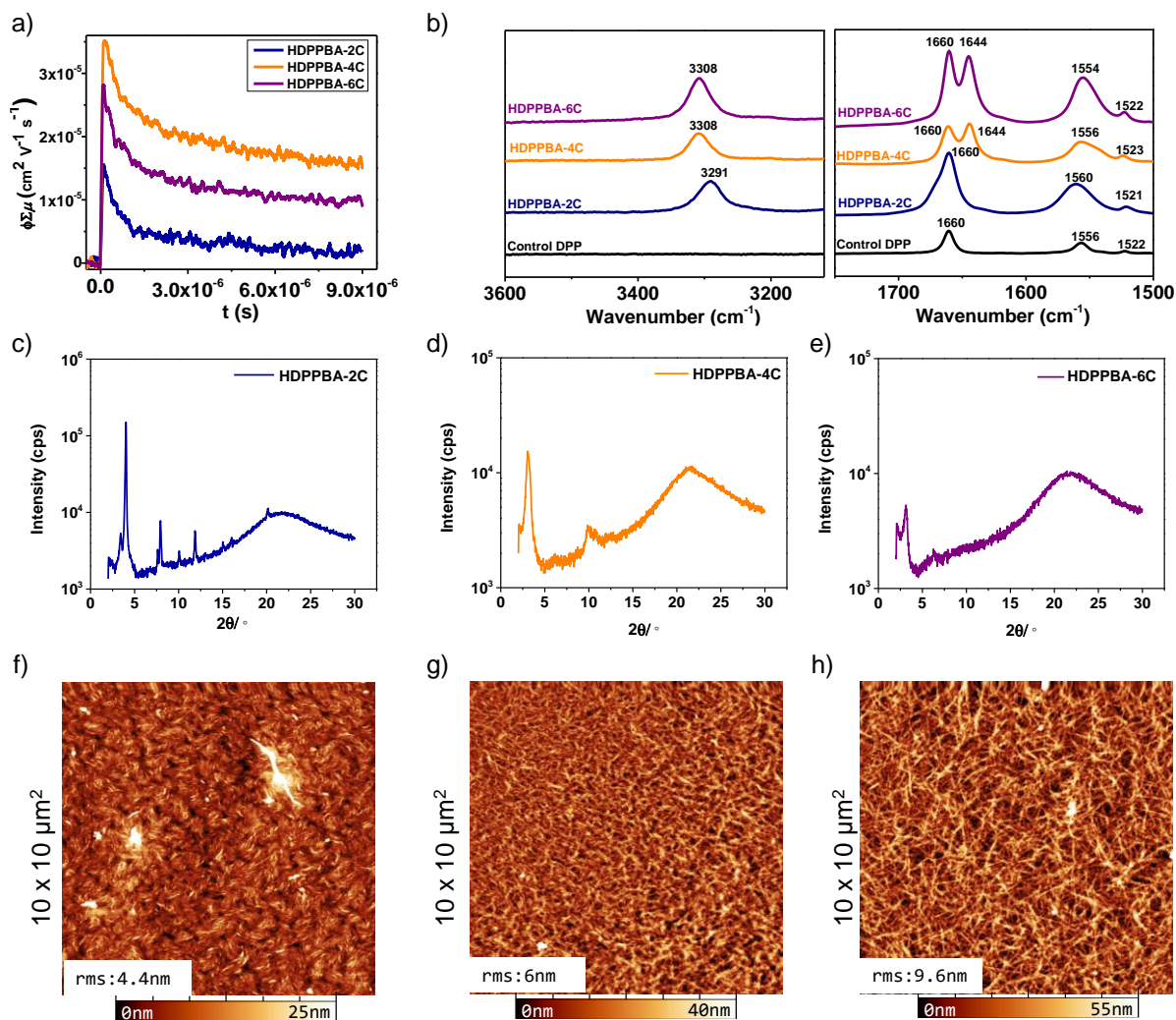


**Figure 4.** a) Kinetic traces of photoconductivity transients of **HDPPBA-2C**, **HDPPBA-4C** and **HDPPBA-6C** measured on thin films deposited by drop-casting CHCl₃ solutions. b) Spectra of Amide A and Amide I and II regions of thin films drop cast from CHCl₃ of **HDPPBA-2C**, **HDPPBA-4C**, **HDPPBA-6C** and spectra of the control molecule unable to form hydrogen bonds.[17] XRD diffractograms thin films of c) **HDPPBA-2C**, d) **HDPPBA-4C**, e) **HDPPBA-6C**. AFM images of thin films cast from CHCl₃ of f) **HDPPBA-2C**, g) **HDPPBA-4C** and h) **HDPPBA-6C**. [**HDPPBA-2C**] = [**HDPPBA-4C**] = [**HDPPBA-6C**] = 2.5 mg/ml in all cases.

15

This is evident in the case of the broad band at 1660 cm$^{-1}$ for **HDPPBA-2C** compared to the band at 1644 cm$^{-1}$ for **HDPPBA-4C** and **HDPPBA-6C** (Figure 4b). The photoconductivity values found, indicate that the suppression of intermolecular hydrogen-bonding causes a negative impact on the charge transport properties and more particularly, in the charge carriers' lifetimes.

**Table 1.** Photoconductivity ($\phi\sum\mu$) values, rate constants ($k$, calculated 3 µs after pulse excitation) and half lifetime ($t_{1/2}$) values for **HDPPBA-2C**, HDPPBA-**4C** and **HDPPBA-6C.**

|  | $\phi\sum\mu$ (cm$^2$V$^{-1}$s$^{-1}$) | k (s$^{-1}$) | t$_{1/2}$ (s) |
|---|---|---|---|
| **HDPPBA-2C** | $1.5 \times 10^{-5}$ | $1 \times 10^5$ | $5 \times 10^{-6}$ |
| **HDPPBA-4C** | $3.5 \times 10^{-5}$ | $4 \times 10^4$ | $2 \times 10^{-5}$ |
| **HDPPBA-6C** | $2.8 \times 10^{-5}$ | $4 \times 10^4$ | $2 \times 10^{-5}$ |

Additionally, X-ray diffraction (XRD) showed that **HDPPBA-2C** forms crystalline structures on thin film (Figure 4c), as pointed by the sharp major peaks at $2\theta$ = 3.4, 4.1 and 7.8°, while the diffractograms of **HDPPBA-4C** and **HDPPBA-6C** (Figure 4d and 4e) show broad peaks indicative of the formation of amorphous structures. The morphology of the films, explored by Atomic Force Microscopy (AFM), (Figure 4f-h) also shows the formation of different types of structures for the three derivatives. **HDPPBA-4C** and **HDPPBA-6C** self-assemble into dense fibrillar networks (Figure 4g and 4h), while **HDPPBA-2C** self-assembles into shorter fiber domains that are not connected to each other (Figure 4f). Additional morphology images are added in the SI for further details (Figures S7, S8 and S9). These results help us further understanding the photoconductivity results since the lack of connection between the domains formed by **HDPPBA-2C** explain the lower values of photoconductivity as well as charge carrier lifetime, even if this derivative is more ordered and crystalline as shown by XRD. In contrast, the **HDPPBA-4C** and **HDPPBA-6C** result to be more efficient in terms of charge transport due to the formation of interconnected structures where the charge

carriers can be more efficiently transported. In summary, all these results agree with the initial studies indicating that interconnection among aggregates is crucial to achieve efficient charge transport, [15,16] even if the aggregates are small and disordered. Furthermore, the results here shown confirm how hydrogen-bonding interactions compete effectively with long-range π–π stacking, improving the electrical performance. This hypothesis is demonstrated also in the case of having extraordinarily small molecules and not only in the case of polymers or more sophisticated oligomers.

## Conclusions

In this work, we show a method to significantly enhance the charge transport capabilities of particularly small π-conjugated segments by strategically positioning hydrogen-bonding units within their molecular structure. Our approach involves the synthesis of thiophene-capped DPP derivatives functionalized with amide units separated from the main conjugated core by alkyl spacers of different lengths. We demonstrate that when the amide units are in close proximity to the DPP core, intermolecular hydrogen-bonding is suppressed, yielding ordered structures lacking connectivity with each other. Conversely, positioning the amide bonds further from the conjugated core promotes intermolecular hydrogen-bonding, giving place to amorphous fibrillar networks that facilitate continuous pathways for charge carrier transport. Consequently, the derivative inhibiting intermolecular hydrogen-boding exhibits markedly inferior photoconductivity values and charge carrier lifetimes one order of magnitude lower. We further confirm that effective charge transport happens through well-interconnected semiconducting domains, even if they are amorphous. More importantly, our findings show how to push the limits of organic electronics by using remarkably small π-conjugated derivatives with enhanced properties achieved by supramolecular chemistry strategies.

## References

[1]    E. D. Głowacki, M. Irimia-Vladu, M. Kaltenbrunner, J. Gsiorowski, M. S. White, U. Monkowius, G. Romanazzi, G. P. Suranna, P. Mastrorilli, T. Sekitani, S. Bauer, T. Someya, L. Torsi, N. S. Sariciftci, *Advanced Materials* **2013**, *25*, 1563–1569.
[2]    C.-H. Huang, N. D. McClenaghan, A. Kuhn, J. W. Hofstraat, D. M. Bassani, *Organic Letters* **2005**, *7*, 3409–3412.

[3]   E. D. Głowacki, H. Coskun, M. A. Blood-Forsythe, U. Monkowius, L. Leonat, M. Grzybowski, D. Gryko, M. S. White, A. Aspuru-Guzik, N. S. Sariciftci, *Organic Electronics* **2014**, *15*, 3521–3528.

[4]   X. Shi, W. Bao, *Frontiers in Chemistry* **2021**, *9*.

[5]   P. Gómez, S. Georgakopoulos, M. Más-Montoya, J. Cerdá, J. Pérez, E. Ortí, J. Aragó, D. Curiel, *ACS Appl. Mater. Interfaces* **2021**, *13*, 8620–8630.

[6]   J. Yao, C. Yu, Z. Liu, H. Luo, Y. Yang, G. Zhang, D. Zhang, *Journal of the American Chemical Society* **2016**, *138*, 173–185.

[7]   T. Aytun, L. Barreda, A. Ruiz-Carretero, J. A. Lehrman, S. I. Stupp, *Chemistry of Materials* **2015**, *27*, 1201–1209.

[8]   D. González-Rodríguez, A. P. H. J. Schenning, *Chem. Mater.* **2011**, *23*, 310–325.

[9]   G. H. Roche, G. Bruckner, D. G. Dumitrescu, J. J. E. Moreau, A. Van Der Lee, G. Wantz, O. J. Dautel, *Adv Elect Materials* **2022**, *8*, 2100265.

[10]  C. Naranjo, S. Adalid, R. Gómez, L. Sánchez, *Angew Chem Int Ed* **2023**, *62*, e202218572.

[11]  M. A. Martínez, A. Doncel-Giménez, J. Cerdá, J. Calbo, R. Rodríguez, J. Aragó, J. Crassous, E. Ortí, L. Sánchez, *J. Am. Chem. Soc.* **2021**, *143*, 13281–13291.

[12]  W. W. Bao, R. Li, Z. C. Dai, J. Tang, X. Shi, J. T. Geng, Z. F. Deng, J. Hua, *Frontiers in Chemistry* **2020**, *8*.

[13]  M. Grzybowski, D. T. Gryko, *Advanced Optical Materials* **2015**, *3*, 280–320.

[14]  G. Martinez, I. Id-boubrik, W. Matsuda, C. C. Carmona-Vargas, K.-I. Hong, C. Munuera, S. Seki, A. Ruiz-Carretero, *Chemistry – A European Journal* **n.d.**, *n/a*, e202400392.

[15]  R. Noriega, J. Rivnay, K. Vandewal, F. P. V. Koch, N. Stingelin, P. Smith, M. F. Toney, A. Salleo, *Nature Materials* **2013**, *12*, 1038–1044.

[16]  T. Adhikari, J.-M. Nunzi, O. Lebel, *Organic Electronics* **2017**, *48*, 230–240.

[17]  N. R. Ávila-Rovelo, G. Martinez, W. Matsuda, S. Sinn, P. Lévêque, D. Schwaller, P. Mésini, S. Seki, A. Ruiz-Carretero, *J. Phys. Chem. C* **2022**, *126*, 10932–10939.

[18]  E. R. Draper, B. Dietrich, D. J. Adams, *Chem. Commun.* **2017**, *53*, 1864–1867.

[19]  M. Cigánek, P. Heinrichová, A. Kovalenko, J. Kučerík, M. Vala, M. Weiter, J. Krajčovič, *Dyes and Pigments* **2020**, *175*, 108141.

[20]  S. Biswas, M. Kumar, A. M. Levine, I. Jimenez, R. V. Ulijn, A. B. Braunschweig, *Chem. Sci.* **2020**, *11*, 4239–4245.

[21]  J. Dhar, N. Venkatramaiah, A. A., S. Patil, *J. Mater. Chem. C* **2014**, *2*, 3457–3466.

[22]  D. T. McQuade, S. L. McKay, D. R. Powell, S. H. Gellman, *J. Am. Chem. Soc.* **1997**, *119*, 8528–8532.

[23]  A. Sarbu, L. Biniek, J.-M. Guenet, P. J. Mésini, M. Brinkmann, *J. Mater. Chem. C* **2015**, *3*, 1235–1242.

[24]  D. J. Moore, M. E. Rerek, R. Mendelsohn, *J. Phys. Chem. B* **1997**, *101*, 8933–8940.

[25]  F. Würthner, T. E. Kaiser, C. R. Saha-Möller, *Angewandte Chemie International Edition* **2011**, *50*, 3376–3410.

[26]  T. E. Kaiser, V. Stepanenko, F. Würthner, *J. Am. Chem. Soc.* **2009**, *131*, 6719–6732.

[27]  J. Matern, Z. Fernández, N. Bäumer, G. Fernández, *Angew Chem Int Ed* **2022**, *61*, e202203783.

[28]  J. Matern, I. Maisuls, C. A. Strassert, G. Fernández, *Angew Chem Int Ed* **2022**, *61*, e202208436.

[29]  M. H. Abraham, R. J. Abraham, *New J. Chem.* **2017**, *41*, 6064–6066.

[30]  M. N. C. Zarycz, C. Fonseca Guerra, *J. Phys. Chem. Lett.* **2018**, *9*, 3720–3724.

[31]  B. Nişancı, A. Daştan, Ö. A. Bozdemir, *Tetrahedron Letters* **2018**, *59*, 3558–3562.

[32]  C. Shao, M. Grüne, M. Stolte, F. Würthner, *Chem. Eur. J.* **2012**, *18*, 13665–13677.

[33]  A. C. Boccia, V. Lukeš, A. Eckstein-Andicsová, E. Kozma, *New J. Chem.* **2020**, *44*, 892–899.

[34]  J. Wu, A. Fechtenkötter, J. Gauss, M. D. Watson, M. Kastler, C. Fechtenkötter, M. Wagner, K. Müllen, *J. Am. Chem. Soc.* **2004**, *126*, 11311–11321.

[35]  K. Zhang, P. Froimowicz, L. Han, H. Ishida, *J. Polym. Sci. Part A: Polym. Chem.* **2016**, *54*, 3635–3642.

[36]  I. Helmers, M. S. Hossain, N. Bäumer, P. Wesarg, B. Soberats, L. S. Shimizu, G. Fernández, *Angew Chem Int Ed* **2022**, *61*, e202200390.

[37]  P. Charisiadis, V. Kontogianni, C. Tsiafoulis, A. Tzakos, M. Siskos, I. Gerothanassis, *Molecules* **2014**, *19*, 13643–13682.

[38]  L.-X. Wang, B.-Q. Hu, J.-F. Xiang, J. Cui, X. Hao, T.-L. Liang, Y.-L. Tang, *Tetrahedron* **2014**, *70*, 8588–8591.

[39]  S. K. Mann, T. N. Pham, L. L. McQueen, J. R. Lewandowski, S. P. Brown, *Mol. Pharmaceutics* **2020**, *17*, 622–631.

[40]  M. Wehner, M. I. S. Röhr, M. Bühler, V. Stepanenko, W. Wagner, F. Würthner, *J. Am. Chem. Soc.* **2019**, *141*, 6092–6107.

[41]  D. S. Philips, K. K. Kartha, A. T. Politi, T. Krüger, R. Q. Albuquerque, G. Fernández, *Angew Chem Int Ed* **2019**, *58*, 4732–4736.

[42]  A. Saeki, Y. Koizumi, T. Aida, S. Seki, *Acc. Chem. Res.* **2012**, *45*, 1193–1202.

[43]  W. Choi, J. Inoue, Y. Tsutsui, T. Sakurai, S. Seki, *Applied Physics Letters* **2017**, *111*, 203302.

[44]  S. Ghosh, R. Raveendran, A. Saeki, S. Seki, M. Namboothiry, A. Ajayaghosh, *ACS Appl. Mater. Interfaces* **2019**, *11*, 1088–1095.

[45]  A. López-Andarias, C. Atienza, J. López-Andarias, W. Matsuda, T. Sakurai, S. Seki, N. Martín, *J. Mater. Chem. C* **2019**, *7*, 6649–6655.

[46]  S. Ghosh, S. Das, A. Saeki, V. K. Praveen, S. Seki, A. Ajayaghosh, *ChemNanoMat* **2018**, *4*, 831–836.

[47]  N. Maity, M. K. Sharma, S. Ghosh, M. K. Huss-Hansen, A. Roy, R. Narayanan, M. Knaapila, W. Matsuda, S. Seki, S. Patil, *ACS Appl. Electron. Mater.* **2023**, *5*, 5093–5102.

[48]  G. Giubertoni, O. O. Sofronov, H. J. Bakker, *Commun Chem* **2020**, *3*, 84.

[49]  A. E. Williams, N. I. Hammer, R. C. Fortenberry, D. N. Reinemann, *Molecules* **2021**, *26*, 4790.

[50]  I. Horcas, R. Fernández, J. M. Gómez-Rodríguez, J. Colchero, J. Gómez-Herrero, A. M. Baro, *Review of Scientific Instruments* **2007**, *78*, 013705.

## Conflicts of interest

The authors declare no conflicts of interest

19

**Experimental**

All reagents and solvents were obtained from commercial suppliers and purified or dried according to standard procedures. Column chromatography was performed on silica gel (VWR Silica 60, particle size 0.040–0.063 mm). Solvents for spectroscopic studies were of spectroscopic grade and used as received. The high-resolution mass was obtained in a MICROTOF II focus (Bruker) with an ESI (electro spray ionization) source. The software used for ion detection is Package Compass Data Analysis (Bruker Daltonics, Bremen, Germany). $^1$H and $^{13}$C spectra were recorded in $CDCl_3$ on a Bruker Avance 400 MHz spectrometer and/or Bruker Avance III HD 500 MHz spectrometer. UV–vis measurements were performed in a conventional quartz cell (light pass 1 mm) on a Cary 5000 UV-Vis-NIR spectrophotometer.

FTIR spectra were recorded with a Vertex 70 from Bruker Optics, equipped with MCT detector and a black-body source. The spectra of the solids were measured by ATR on diamond. The solutions were studied in cells from Specac Pike with KBr NaCl windows. The spectra were compensated from $CO_2$ and moisture with OPUS from Bruker. The solvent intensities were measured separately and subtracted.

The surface morphology of samples was analyzed using a commercial AFM system and software from Nanotec[50] operating in ambient conditions. Topographic images were acquired in dynamic mode, with a commercial tip from Nanosensors, exciting the tip at its resonance frequency of 75 kHz. The samples were prepared by drop casting 20 μL chloroform solutions at a 2.5 mg/ml concentration on silicon wafers covered with 290 nm of $SiO_2$.

Cyclic voltammetry measurements were carried out under an atmosphere of argon using a three-electrode arrangement in a single compartment cell. A platinum disc working electrode, a platinum wire counter electrode and a non-aqueous $Ag/Ag^+$ reference electrode were used in the cell using an Ossila potentiostat. Redox potentials are quoted versus the ferrocenium-ferrocene couple, which was used as

an internal reference, 100 mV/s scan rate. $CH_2Cl_2$ (dried and degassed) was utilized as solvent with tetrabutylammonium hexafluorophosphate ($TBAPF_6$, 0.1 M) employed as supporting electrolyte.

HOMO and LUMO levels were calculated using the equations:

$E_{HOMO}$ = - ($E_{onset}$(ox) + 4.8 [eV]) and $E_{LUMO}$ = -($E_{onset}$(red) + 4.8 [eV]).

The band gap is calculated using the equation

$Eg$ = $E_{HOMO}$ - $E_{LUMO}$ [eV].

Charge carrier mobilities were evaluated by FP-TRMC at room temperature. The thin films of samples were fabricated by drop-cast method onto quartz substrates ($9 \times 40$ mm$^2$, 1 mm thick). Charge carriers were injected into the materials via photo-ionization with a third harmonic generation ($\lambda = 355$ nm) of a Spectra Physics model INDI-HG Nd:YAG laser pulses at 10 Hz with a pulse duration of ca. 5 ns. The photon density of a 355 nm pulse was modulated from $9.1 \times 10^{15}$ photons cm$^{-2}$ pulse$^{-1}$. A GUNN diode oscillator model MMP-3015 (Nakadai S.S. Japan) was used as the microwave power source. The microwave frequency and power were set at ~9.1 GHz and 3 mW, respectively, and guided into a microwave cavity. The $Q$-factor of the microwave cavity loaded with the sample was 2200, and the substrates with the compound films were set at the point of electric field maximum. The reflected power of the probing microwave, picked up by a GaAs crystal–diode with Schottky–barriers (rise time < 1 ns), was monitored by a Tektronics model TDS3054 digital oscilloscope. The observed change in the reflected microwave power ($\Delta P_r$) was normalised with the steady reflection of the microwave from the cavity ($P_r$), and converted directly into the product of a photocarrier generation yield ($\square$) and the sum of photo-generated electron/hole mobilities ($\square\square$),

$$\phi\Sigma\mu = 1/(eI_0F_{light}) \times (1/A) \times (\Delta P_r/P_r), \qquad\qquad \square\square 1)$$

where $e$, $A$, $I_0$, and $F_{light}$ are elementary charge, sensitivity factor (S$^{-1}$ cm), incident photon density of the excitation laser (photon cm$^{-2}$), and filling factor (cm$^{-1}$), respectively. The value of $F_{light}$ was calculated based on the overlap of the area of photo-carrier injection (presumed to be proportional to the absorbance of excitation light by the sample film) with electric field strength distribution in the cavity derived from a calculation code of CST Microwave Studio from AET Inc.